

Chapter 2

Instrumentation

This chapter discusses the telescopes used to take the observations presented and used in this work. The data reduction processes for SCUBA-2 data and Herschel observations are described, as are the methods used to make data from SCUBA-2 and Herschel comparable. Parts of the discussions of masking and of convolution kernels were published by Pattle et al. (2015), *Monthly Notices of the Royal Astronomical Society*, vol. 450, p. 1094.

2.1 The James Clerk Maxwell Telescope

The James Clerk Maxwell Telescope (hereafter, JCMT), located near the summit of Mauna Kea, Hawai'i, is an altitude-azimuth-mounted Cassegrain/Nasmyth telescope with a 15 m parabolic primary antenna, and as such is the largest single-dish sub-millimetre observatory in the world. The telescope is shown in Fig. 2.1. The JCMT is optimised to operate in the $\sim 350\text{--}1000\,\mu\text{m}$ wavelength range. The JCMT has a rotating tertiary mirror which allows the beam to be directed to a variety of instruments. There are currently four fully commissioned instruments operating at the JCMT: SCUBA-2, HARP-B, Receiver A and Receiver W¹. Data from two of these, SCUBA-2 and HARP-B, are used in this work.

The JCMT has historically been operated by the Joint Astronomy Centre in Hilo, Hawaii and funded by the UK, Canada and the Netherlands. In early 2015 telescope operations were taken over by the East Asian Observatory (EAO), a consortium of universities from Taiwan, China, Japan and South Korea. The UK and Canada remain partners in the JCMT.

¹This was correct at the time of writing. The POL-2 polarimeter has subsequently been commissioned.

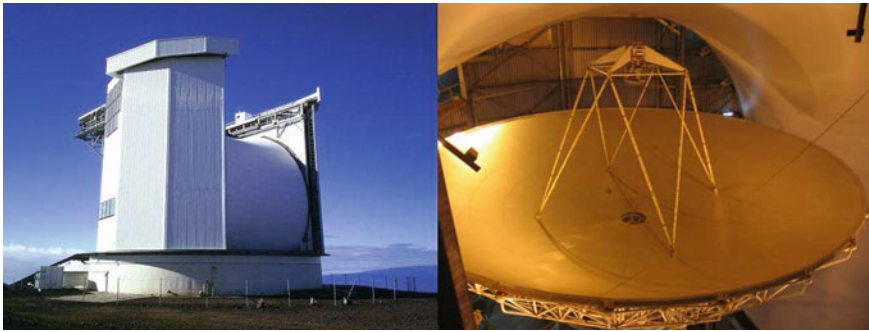


Fig. 2.1 Exterior (*left*) and interior (*right*) views of the James Clerk Maxwell Telescope. Exterior view shows the Goretex shield protecting the telescope, and the rotating carosel on which the telescope is mounted. Interior view shows the telescope primary antenna and secondary mirror. Images © Joint Astronomy Centre. Reproduced with permission

2.1.1 SCUBA-2

The SCUBA-2 (Submillimetre Common-User Bolometer Array 2) instrument is a 10000 pixel camera on the JCMT. SCUBA-2 observes in two wide wavelength bands, centred on $450\ \mu\text{m}$ and $850\ \mu\text{m}$, at effective resolutions of $9.6''$ and $14.1''$ respectively (Holland et al. 2013). The two wavebands are observed simultaneously by means of a dichroic beam splitter. The key components of SCUBA-2, and their operating temperatures, are shown in Fig. 2.2. Incoming light is directed into SCUBA-2 by the JCMT tertiary mirror. It is then passed through a series of thermal edge (TE) filters and low-pass (LP) frequency filters: a $5\ \mu\text{m}$ TE filter at room temperature; 10 and $20\ \mu\text{m}$ TE filters; a $270\ \mu\text{m}$ ($1.1\ \text{THz}$) LP filter at $50\ \text{K}$; a $30\ \mu\text{m}$ TE filter; and a $303\ \mu\text{m}$ ($990\ \text{GHz}$) LP filter at $4\ \text{K}$. Finally, the light enters the $1\ \text{K}$ box. The light is then passed through $345\ \mu\text{m}$ ($870\ \text{GHz}$) and $310\ \mu\text{m}$ ($967\ \text{GHz}$) LP filters, before being passed through the dichroic beam splitter. The transmitted portion of the light (with wavelength range $769\text{--}1000\ \mu\text{m}$) is then passed through a $714\ \mu\text{m}$ ($420\ \text{GHz}$) LP filter and an $850\ \mu\text{m}$ bandpass filter before reaching the $850\ \mu\text{m}$ focal plane of the camera. The reflected ($400\text{--}526\ \mu\text{m}$) portion of the light is passed through a $625\ \mu\text{m}$ ($480\ \text{GHz}$) high-pass frequency filter, a $450\ \mu\text{m}$ bandpass filter and a $385\ \mu\text{m}$ ($779\ \text{GHz}$) LP filter before reaching the $450\ \mu\text{m}$ focal plane. The focal planes have an operating temperature of approximately $0.1\ \text{K}$.

2.1.1.1 Data Acquisition

A SCUBA-2 focal plane unit is shown in Fig. 2.3. The focal planes at each wavelength are populated with four rectangular sub-arrays, each of which contains 40×32 bolometers. The total focal plane array footprint on the sky is approximately $600'' \times 600''$. Each bolometer is a thermal absorber coupled to a superconducting transition

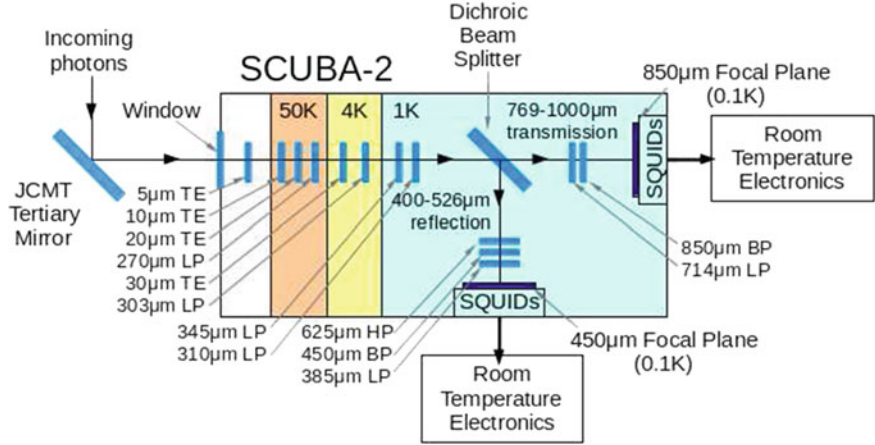
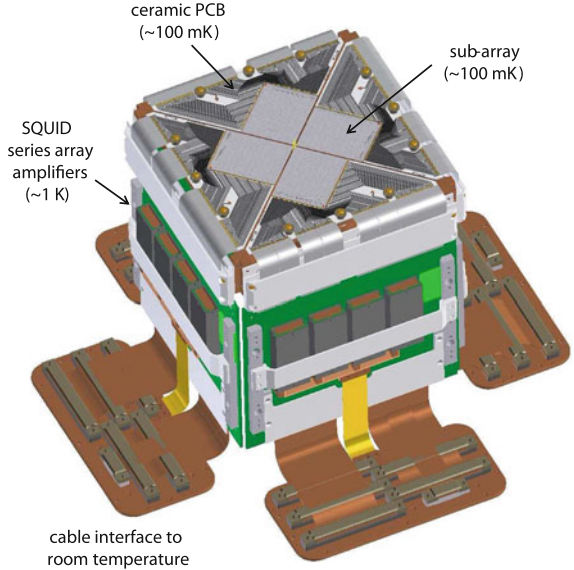


Fig. 2.2 A schematic diagram of SCUBA-2, showing the operating temperatures of the principal components

Fig. 2.3 Layout of a SCUBA-2 focal plane unit. Holland et al. (2013), “SCUBA-2: The 10 000 Pixel Bolometer Camera on the James Clerk Maxwell Telescope”, Monthly Notices of the Royal Astronomical Society, vol. 430, p. 2513, Figure 1. Reproduced with the permission of Oxford University Press



edge sensor (TES). A TES is a thin superconducting film kept at a temperature very near to its transition temperature. If raised above its transition temperature it ceases to be a superconductor, and hence its resistance increases substantially, and the current in the circuit decreases equivalently. The TES is connected in parallel with a fixed resistor and in series with an inductor; this inductor is inductively coupled to a superconducting quantum interference device (SQUID; a sensitive magnetometer which utilises the Josephson effect to produce a voltage proportional to an applied

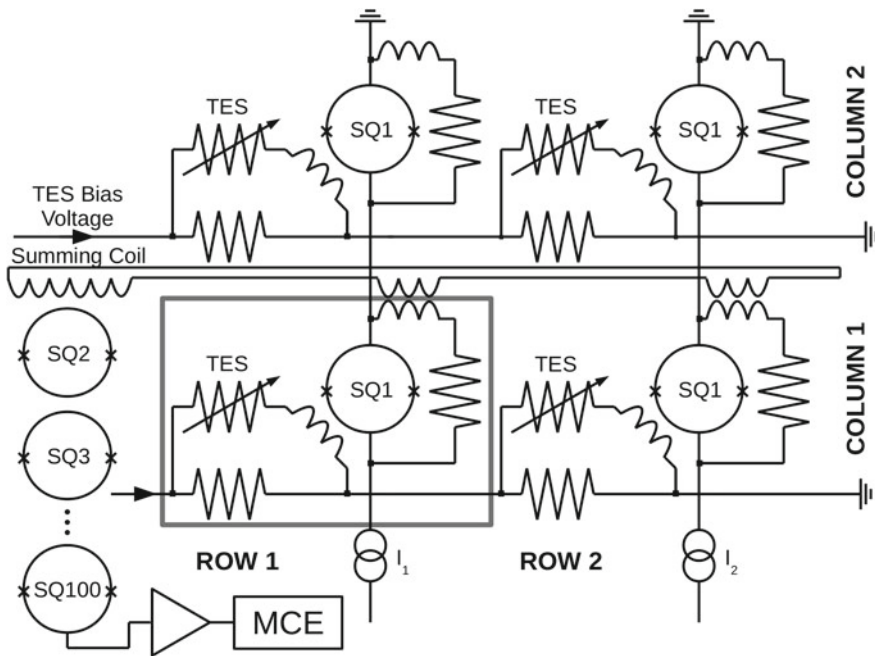


Fig. 2.4 A simplified circuit diagram (after Holland et al. 2013), showing the configuration of components within each subarray of SCUBA-2. The area enclosed by the *box* shows the components associated with one pixel

magnetic field). The changing magnetic field resulting from the change in current in the TES circuit is detected by the SQUID.

A fixed resistor and inductor are connected in parallel with the SQUID, and the circuit is inductively coupled to a further SQUID circuit, so that the changing voltage across the SQUID can be amplified. The initial magnetic field is amplified by a chain of 100 SQUIDS, creating an output current large enough to be digitised. Each bolometer has its own TES and SQUID; thereafter, each column of 32 bolometers has a common chain of SQUIDS. Figure 2.4 shows a simplified circuit diagram indicating the layout of components within a subarray. The signal from each of the 40 rows is read in turn, at a frequency of 12 kHz, and then resampled to 200 Hz, i.e. a sample is taken every 3'' at the maximum scanning speed of 600''/s. This ensures that there are approximately 3 samples per 450 μm diffraction-limited FWHM, and hence that the 450 μm data is better than Nyquist-sampled.

Along with the 40 rows of detectors on each focal sub-array, there is an additional 41st row of SQUIDS which are not connected to TESs. These 'dark SQUIDS' measure and track non-thermal noise common to each of the sub-array's amplifier chains.

The conversion between input power and output current is determined by flat-field observations, taken immediately before each set of science observations. In a

Table 2.1 SCUBA-2 beam properties, from Dempsey et al. (2013)

	450 μm	850 μm
FWHM primary beam (arcsec)	7.9	13.0
FWHM secondary beam (arcsec)	25	48
Primary beam amplitude	0.94	0.98
Secondary beam amplitude	0.06	0.02
Primary beam volume	0.6	0.78
Secondary beam volume	0.4	0.22
Beam FCF ($\text{Jy pW}^{-1} \text{ arcsec}^{-1}$)	4.71 ± 0.50	2.34 ± 0.08
Peak FCF (Jy pW^{-1})	491 ± 67	537 ± 26

flat-field observation, the pixel heaters are ramped, and for these known input power values, the output current response is measured.

After being amplified, the signal is passed to room-temperature electronics known as Multi-Channel Electronics (MCE), before being passed to a data acquisition computer (one for each sub-array), along with information about the state of the instrument. From there, the data are archived, prior to reduction.

The output power must be corrected for atmospheric extinction. This is determined using the JCMT Water Vapour Monitor (WVM) to track opacity variation along the line of sight.

Finally, a flux conversion factor (FCF) must be applied to convert from power to astrophysical flux. Standard calibrators are regularly measured for this purpose. The primary calibrators for SCUBA-2 are Mars and Uranus, both of which have a $\sim 5\%$ uncertainty in their model fluxes (Dempsey et al. 2013). There are a number of secondary calibrators, which are observed when the primary calibrators are not visible. The standard peak FCF values are $491 \pm 67 \text{ Jy/pW}$ at $450 \mu\text{m}$ and $537 \pm 26 \text{ Jy/pw}$ at $850 \mu\text{m}$ (Dempsey et al. 2013).

2.1.1.2 PONG Observing Mode

Observations made as part of the JCMT GBS used fully sampled circular regions. Other than some data taken as part of the Science Verification programme, observations were $30'$ in diameter. All observations were taken using the ‘PONG’ observing mode (Holland et al. 2013), in which the area of even coverage within the observation is maximised. This is done by defining the map as a square region and tracking the telescope across this region, ‘bouncing’ off the walls of the square as shown in Fig. 2.5. Once the pattern is completed and the square has been covered, the map is rotated and the pattern is repeated.

This observing mode allows large areas to be mapped, and permits the robust recovery of structure on scales up to the array size ($600''$). Figure 2.6 shows the region

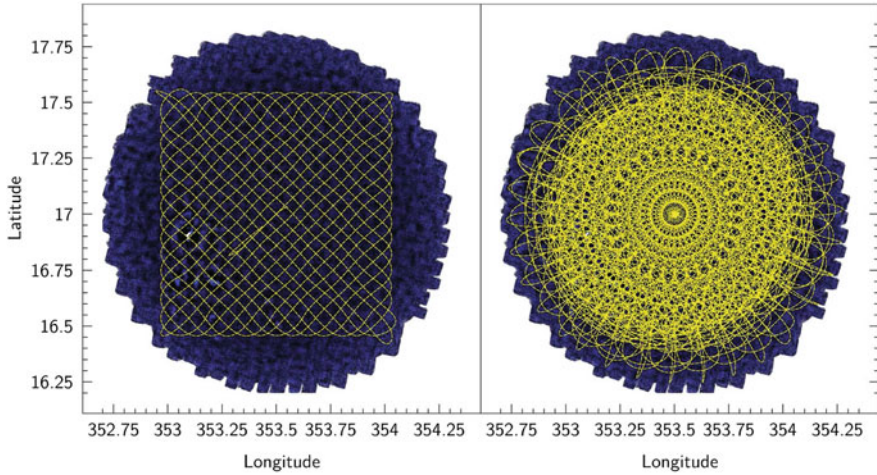


Fig. 2.5 The SCUBA-2 PONG observing mode, shown on a 30 arcminute diameter field. The *left-hand panel* shows the telescope track for a single pong pattern; the *right-hand panel* shows the track for a full PONG1800 observation. Holland et al. (2013), “SCUBA-2: The 10 000 Pixel Bolometer Camera on the James Clerk Maxwell Telescope”, Monthly Notices of the Royal Astronomical Society, vol. 430, p. 2513, Figure 11. Reproduced with the permission of Oxford University Press

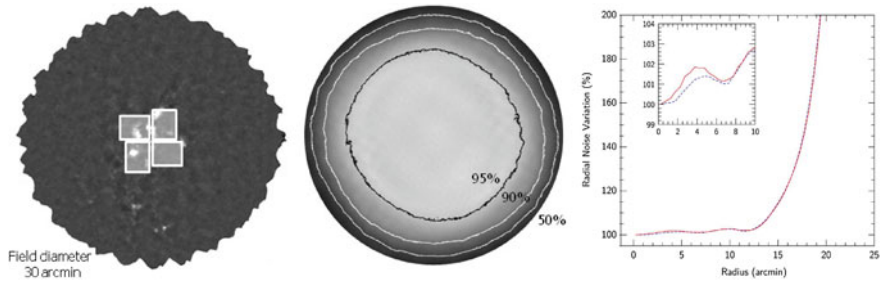


Fig. 2.6 The *leftmost panel* shows a 30 arcmin PONG observation, with the array size overlaid. The *central panel* shows the exposure time of the observations, with contours showing the radii of 95, 90 and 50% of the peak value. The *rightmost panel* shows the percentage increase in RMS map noise as a function of radius. Holland et al. (2013), “SCUBA-2: The 10 000 Pixel Bolometer Camera on the James Clerk Maxwell Telescope”, Monthly Notices of the Royal Astronomical Society, vol. 430, p. 2513, Figure 12. Reproduced with the permission of Oxford University Press

of even coverage of a PONG1800 observation (a 30'-diameter region). Overlapping observations can be mosaiced in order to create continuous maps with large areas of even coverage. The PONG observing pattern is designed to modulate the sky signal as much as possible, both spatially (i.e. by scanning the same region at different position angles) and temporally (by scanning the same region at different speeds). This modulation is necessary in order to maximise the recovery of large-scale structure, due to the presence of slowly-varying signals, both spatially and temporally, in

the data. These slowly-varying signals—atmospheric signal, variations in extinction, and instrumental $1/f$ noise—can be confused with astrophysical emission, hence the necessity for signal modulation. The methods by which the astrophysical signal is distinguished from these other components are discussed in Sect. 2.1.2, below.

2.1.1.3 Weather Bands

The JCMT measures weather quality in terms of the atmospheric opacity at 225 GHz, and categorises weather quality into five grades, with Grade 1 being the best observing conditions. The definitions of the different weather bands in terms of 225 GHz opacity (τ) and millimetres of precipitable water vapour along the telescope’s line of sight (PWV) are listed in Table 2.2. All GBS data were taken in Grade 1 or Grade 2 weather. Grade 1 weather gives atmospheric transmission of better than 82% at 850 μm and better than 28% at 450 μm , and is necessary for observing faint structure at 450 μm . Only key regions were observed in this weather grade. Grade 2 weather might typically give atmospheric transmissions of $\sim 77\%$ at 850 μm and $\sim 19\%$ at 450 μm ; these transmission values allow high-quality 850 μm observations, but only bright 450 μm emission will be recoverable. (Note that atmospheric transmission at 850 μm is higher than that at 450 μm .)

2.1.2 SCUBA-2 Data Reduction

SCUBA-2 data reduction is performed using an iterative mapmaking routine, *makemap* in SMURF (Chapin et al. 2013). The data reduction process is described in detail by Chapin et al. (2013), and summarised here. An overview of the process is shown in Fig. 2.7.

The first step in the mapmaking process is to read the data files into memory and concatenate them into a set of continuous time series for each subarray. A flat-field correction is then applied, determined by the closed-shutter instrument response measurements taken immediately prior to the observation (see above). The data are then down-sampled to match the requested pixel size in the final map. The data are

Table 2.2 JCMT weather bands

Grade	Definition	τ	PWV (mm)
1	Very dry	<0.05	<0.83
2	Dry	$0.05\text{--}0.08$	$0.83\text{--}1.58$
3	Medium	$0.08\text{--}0.12$	$1.58\text{--}2.58$
4	Wet	$0.12\text{--}0.2$	$2.58\text{--}4.58$
5	Very wet	>0.2	>4.58

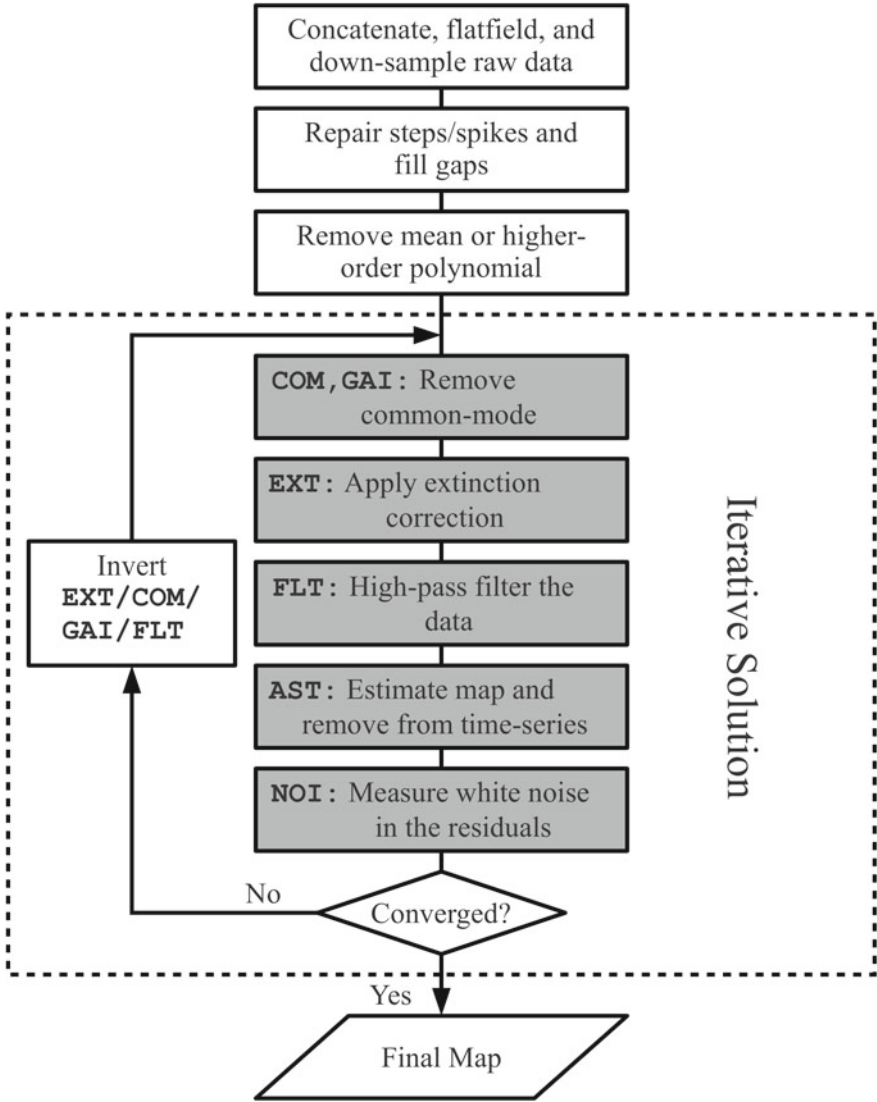


Fig. 2.7 The SCUBA-2 data reduction process. Chapin et al. (2013), “SCUBA-2: iterative map-making with the Sub-Millimetre User Reduction Facility”, Monthly Notices of the Royal Astronomical Society, vol. 430, p. 2545, Figure 6. Reproduced with the permission of Oxford University Press

then cleaned: noise spikes in the data are identified and removed, steps in the time series (likely the result of cosmic ray events) are corrected for, and any gaps in the time series are filled. Gaps are filled by interpolating between the start and end values of the gap, with Gaussian noise added to the interpolated values.

The total sky signal observed by SCUBA-2 is modelled as having four components: astrophysical signal (AST), atmospheric, or common-mode, signal (COM), low-frequency $1/f$ noise (FLT), and other noise (NOI). The astrophysical signal is recovered by iteratively modelling each of these components.

$$\text{Cleaned Value} = \text{COM} + \text{FLT} + \text{AST} + \text{Residuals} \quad (2.1)$$

The degeneracy between these components makes it necessary to iteratively model each of these components, in order to minimise the residuals. The residual term consists of both uncorrelated white noise (NOI), which cannot be minimised, and correlated components, which should in fact be assigned to the COM, AST or FLT models. The atmospheric (COM) signal is the mean of all bolometer values at each time-slice, on the assumption that there is no variation in signal from the atmosphere across the array footprint. The COM is then converted into a gain model (GAI), being weighted by the gain and zero-level offset for each bolometer. This GAI model is then subtracted from the cleaned data.

After the common-mode signal has been removed from the data, the extinction correction (EXT) is applied. This is a constant multiplicative scaling factor derived from the WVM, but is applied in each iteration after the COM model has been applied in order to avoid amplifying small errors.

The low-frequency noise (FLT) is estimated for each bolometer. This is done by Fourier transforming the time series data for each bolometer, applying a high-pass filter, and inverting the Fourier transform. This step removes residual $1/f$ noise remaining after the common-mode signal has been removed.

The signal map is then estimated, along with an associated variance map. The data are nearest-neighbour resampled onto a map grid: for each pixel, the brightness is estimated to be the weighted average of the good bolometer data samples that fall within that pixel. For the first iteration of the mapmaker, the weights of each bolometer data sample are set to 1; thereafter, the weights are given by the inverse variance expected from the bolometer white noise level.

For the i th pixel in the map, contributed to by bolometer data samples b_j with weights w_j , the brightness $M(x_i, y_i)$ is given by

$$M(x_i, y_i) = \frac{\sum_j w_j b_j}{\sum_j w_j} \quad (2.2)$$

and the variance $v(x_i, y_i)$ in the pixel is given by

$$v(x_i, y_i) = \frac{\sum_j w_j \sum_j w_j b_j - \left(\sum_j w_j b_j\right)^2}{N \left(\sum_j w_j\right)^2} \quad (2.3)$$

where N is the total number of bolometer samples that fall within the pixel.

The white noise (NOI) component is estimated from the residuals in the second iteration after the AST model has been subtracted from the time series data. The NOI model is then fixed, to prevent the weights of each bolometer diverging, and to allow a fixed reference against which to estimate the χ^2 value of the map.

This is the final stage in the iterative part of the mapmaking process. To begin the next iteration, the FLT, EXT and COM models are inverted, leaving the initial cleaned data with the current AST model subtracted. Unless the map convergence criterion has been met (discussed below), the iterative process then begins again with modelling of the common mode.

2.1.2.1 Convergence

After the i th iteration of the mapmaker, the signal map is given by

$$\text{Map}_i = (\text{Cleaned Data} - \text{AST}_{i-1}) - \text{COM}_i - \text{FLT}_i + \text{AST}_i \quad (2.4)$$

and the mean map change is given by

$$(\text{Mean Map Change})_i = \frac{1}{N_i} \sum_j \left| \frac{M_{j,i} - M_{j,i-1}}{\sqrt{v_{j,i}}} \right| \quad (2.5)$$

where $M_{j,i}$ is the map signal in the j th pixel enclosed by the mask (discussed below) after the i th iteration of the mapmaker, $\sigma_{j,i}$ is the standard deviation in this pixel, and N_i is the total number of pixels enclosed by the mask in iteration i . The mapmaking process is ended when the mean map change reaches a specified value; in the case of the GBS, this is 0.001, or a mean change of 0.1% across the map.

2.1.2.2 Masking

The degeneracy between AST, COM and FLT signal can, without some constraints placed on the mapmaker, lead to several defects in the output map. The degeneracy between AST and COM can lead to what is in fact common-mode signal being assigned to the AST model. This causes the AST model to diverge, resulting in large ‘blooms’ of emission across the map. The FLT high-pass filtering applied to the time-stream data can also lead to ringing around bright sources, if they are not correctly assigned to the AST model.

The solution to these issues is to provide a ‘mask’ for the data: information as to whether or not any given pixel is expected to contain astrophysical signal. At the end of each iteration, all pixels in the map outside the masked region are set to zero, and the AST model is updated accordingly. This prevents small amounts of COM signal mistakenly assigned to the AST model in poorly constrained low signal-to-noise

regions of the map from diverging in subsequent iterations. On the final iteration of the mapmaker, the pixels outside the mask are not set to zero.

In order to be able to define a mask without requiring a priori knowledge of the astrophysical signal, the GBS method for data reduction requires the data reduction process to be repeated. For the first reduction, an ‘automask’ is generated as a part of the mapmaking process. Here, the mask is determined iteratively, based on the signal-to-noise in the data. In each iteration, for each pixel, the signal-to-noise is taken to be

$$\text{Signal-to-Noise}(x_i, y_i) = \frac{M(x_i, y_i)}{\sqrt{v(x_i, y_i)}}. \quad (2.6)$$

Pixels with a signal-to-noise greater than 5 are included in the mask.

The map resulting from this process provides a good first approximation to the real astrophysical signal. However, the mask can be improved by using the repeat observations taken at each observing position. Once all the available data have been automask-reduced, the observations can be co-added and, if overlapping observing positions have been chosen, mosaiced. From this mosaic, a higher-quality signal-to-noise mask can be created. With this fixed ‘external’ mask (or ‘extmask’), the data reduction process is repeated for each observation, now with a clear and consistent definition of the pixels which contain signal which may be assigned to the AST model.

For the GBS Internal Release 1 data, the typical mask-making process was

1. Create a signal-to-noise map from the automask-reduced signal and variance maps.
2. Threshold the signal-to-noise map at a chosen value (typically 5, for IR1), setting everything above this value to 1 and everything below it to 0.
3. Smooth this mask with a Gaussian kernel, typically in the range FWHM = 5–10 pixels.
4. Threshold the mask again at a chosen value, typically 0.05, setting everything above this value to 1 and everything below it to zero.
5. Inspect the mask, manually removing any masked regions that are the result of noise spikes (typically, these are found around the map edges).

As part of the testing for the Internal Release 2 reduction, it was found that smoothing the mask could in some fields produce defects in the map where in regions of lower signal-to-noise, included in the mask due to the smoothing, spurious AST signal was allowed to grow. For the IR2 reduction, typically only the first and second steps of the above process were applied, with a signal-to-noise cut of zero being used.

The external mask used in the IR1 reduction of the SCUBA-2 Ophiuchus data is shown in Fig. 2.8. A subsection of the mask used in the IR2 reduction of the same data, for the subregion L1688, is shown in Fig. 2.9.

The data used in Chaps. 3 and 4 of this work—observations of the Ophiuchus (Chap. 3) and Taurus (Chap. 4) molecular clouds—were reduced using the IR1 method. The data used in Chap. 5—observations of the Cepheus region—were

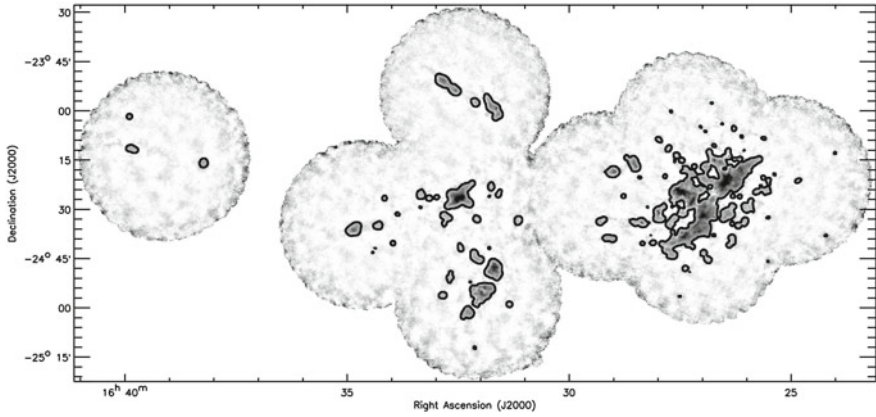


Fig. 2.8 The *black contour* shows the edges of the IR1 mask for Ophiuchus, defining regions of significant emission. This figure appears in Pattle et al. (2015), Monthly Notices of the Royal Astronomical Society, vol. 450, p. 1094

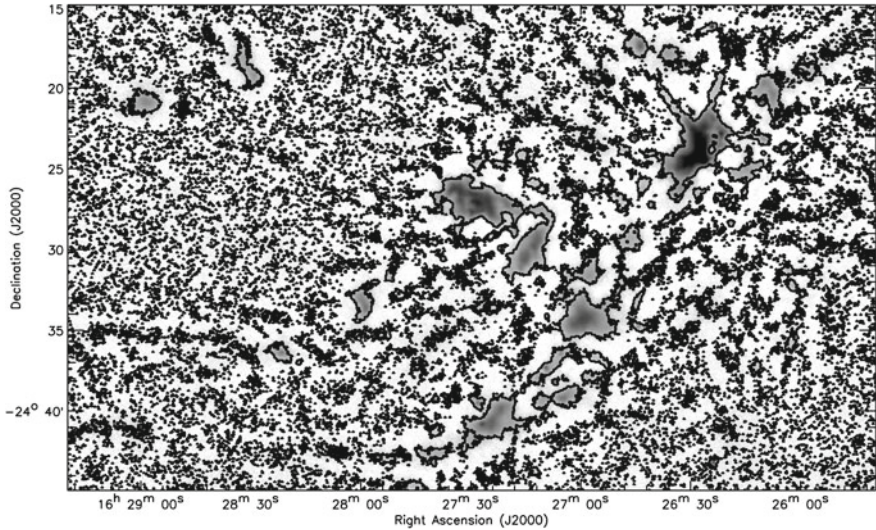


Fig. 2.9 The *black contour* shows the edges of the IR2 mask for the L1688 region of Ophiuchus, defining regions of significant emission

reduced using the IR2 method. This situation arose for historical reasons, since the first two data sets were published before IR2 was available.

2.1.3 HARP-B and ACSIS

HARP-B (Heterodyne Array Receiver Program for the B-Band) is a 4×4 element heterodyne focal plane array receiver, sensitive in the range 325–375 GHz (~ 800 – $925 \mu\text{m}$), with an angular resolution of $14''$ at 345 GHz, or $879 \mu\text{m}$ (Buckle et al. 2009). Its backend is the Auto-Correlation Spectral Imaging System, ACSIS. The spectral range of HARP-B is shown in Fig. 2.10, along with astrophysically important observable transitions.

The 16 HARP-B detectors are arranged in a 4×4 grid with a spacing of $30''$ between the detectors, resulting in an undersampled field of view of $104'' \times 104''$ at 345 GHz. In order to produce fully-sampled maps of large areas, a scanning (also known as on-the-fly mapping or rastering) observing mode is used, in which the telescope is moved steadily across the target field, with data being integrated continuously. The HARP-B array is rotated 14.48° relative to the scan direction, resulting in a sample spacing of $7.3''$ perpendicular to the scan direction. The array and scan pattern are shown in Fig. 2.11.

HARP-B covers the whole target field as rapidly as possible in order to minimise the effect of variations in sky transmission, pointing changes and calibration drifts. Each observation is repeated multiple times, and the resulting maps are co-added to increase the signal-to-noise ratio. Co-adding several rapidly-observed maps reduces calibration uncertainties across the final map. At the end of every one or every few rows in an observation, the telescope is ‘nodded’ to a specified off-source reference

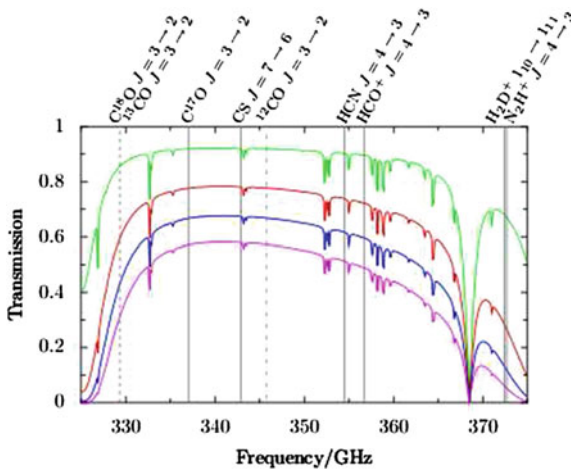


Fig. 2.10 Atmospheric transmission in JCMT weather bands 1–4 across the HARP-B observing range (325–375 GHz; 800 – $925 \mu\text{m}$), with frequently-observed transition frequencies marked. Buckle et al. (2009), “HARP/ACIS: a submillimetre spectral imaging system on the James Clerk Maxwell Telescope”, *Monthly Notices of the Royal Astronomical Society*, vol. 399, p. 1026, Figure 20. Reproduced with the permission of Oxford University Press

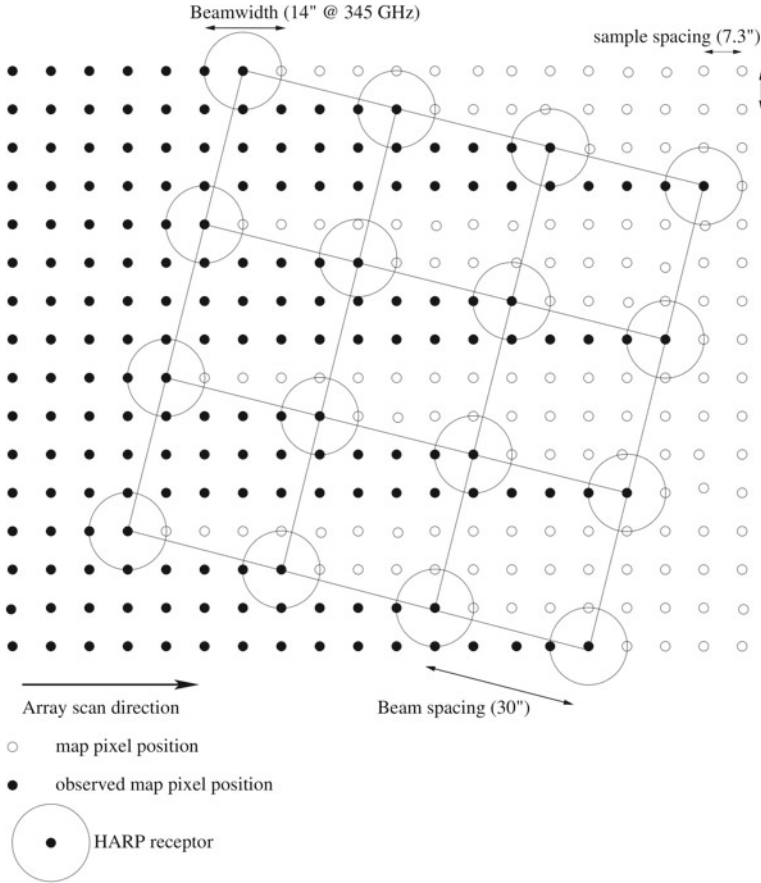


Fig. 2.11 HARP-B scanning observing mode, demonstrating how fully sampled coverage is achieved using an undersampled array. Buckle et al. (2009), “HARP/ACSIS: a submillimetre spectral imaging system on the James Clerk Maxwell Telescope”, *Monthly Notices of the Royal Astronomical Society*, vol. 399, p. 1026, Figure 17. Reproduced with the permission of Oxford University Press

position, at which an off-source signal is observed simultaneously for each pixel. Using these off-source observations, most instrumental and atmospheric effects can be removed from the data. HARP-B operates as a single-sideband instrument; the unwanted frequency range is filtered (attenuated by a factor of 10–50) before the signal reaches the mixer. This is done in order to decrease system temperatures and to increase calibration accuracy.

In order to mitigate noise variations due to missing detectors or variations in detector performance, two independent maps can be made of a field, with the telescope scanning in orthogonal directions. These maps are then co-added. This technique, used in GBS HARP-B observations, is known as basket-weaving.

ACSIS allows either wide-band or high-resolution spectra to be observed, and also allows the frequency range to be split into sub-bands. HARP-B has 16 outputs while ACSIS has 32 inputs: this allows two transitions with similar frequencies to be observed simultaneously (e.g. the $^{13}\text{CO } J=3 \rightarrow 2$ and $\text{C}^{18}\text{O } J=3 \rightarrow 2$ transitions), or for a transition to be simultaneously observed in both wide-band and high-resolution modes.

HARP-B data are reduced using Starlink project software. The data reduction process is described in detail by Curtis et al. (2010). Starlink KAPPA routines (Currie et al. 2008) are used to mask poorly performing detectors. The data cube is made using the SMURF routine *makecube* (Jenness et al. 2008). It is necessary to perform a ‘self-flat’ or ‘de-stripping’ of the data, where systematic calibration differences between HARP-B detectors are eliminated—described in detail by Curtis et al. (2010). Finally, KAPPA routines are used to remove linear baselines from the cube and to crop the map edges.

HARP-B CO data are calibrated relative to the sources IRC+10216, CRL2688 and CRL618. Buckle et al. (2009) estimate a calibration accuracy for HARP-B of $\sim 20\%$.

2.1.4 Carbon Monoxide Contamination of SCUBA-2 Data

SCUBA-2 850- μm data may be substantially contaminated by the $\text{CO } J=3 \rightarrow 2$ transition (Drabek et al. 2012) which, with a rest wavelength of 867.6 μm , is covered by the SCUBA-2 850- μm filter—half-power bandwidth 85 μm (Holland et al. 2013). The SCUBA-2 850- μm filter is a broad-band filter, intended to measure continuum emission. However, the $\text{CO } J=3 \rightarrow 2$ transition is excited in the low-to-medium-density material in molecular clouds (Bolatto et al. 2013, and references therein), and hence can contribute a significant fraction of the measured emission in the 850- μm band in SCUBA-2 observations of molecular clouds. Drabek et al. (2012) estimate that the contribution to the measured 850- μm continuum emission from CO is generally $\leq 20\%$ in GBS SCUBA-2 850- μm observations, but can reach $\sim 80\%$ in outflow-dominated regions.

Where SCUBA-2 and HARP-B CO data exist for the same observing position, CO contamination can be corrected for by re-reducing each of the 850- μm observations with the integrated ^{12}CO data added to the SCUBA-2 bolometer time series as a negative signal.

2.2 The Herschel Space Observatory

The Herschel Space Observatory (hereafter, Herschel) was a space observatory with a 3.5 m diameter Cassegrain telescope, which orbited the second Sun-Earth Lagrangian point (Pilbratt et al. 2010). The telescope, a European Space Agency (ESA) mission with contributions from the National Aeronautics and Space Administration (NASA), was launched in May 2009 and ceased operations upon running out of helium coolant in April 2013.

Herschel carried three instruments: SPIRE (Spectral and Photometric Imaging REceiver—Griffin et al. 2010); PACS (Photodetector Array Camera and Spectrometer—Poglitsch et al. 2010) and HIFI (Heterodyne Instrument for the Far Infrared—de Graauw et al. 2010). Data taken using SPIRE and PACS are used in this work. SPIRE consisted of a photometer operating simultaneously at $250\text{ }\mu\text{m}$, $350\text{ }\mu\text{m}$ and $500\text{ }\mu\text{m}$ at resolutions of $18''$, $25''$ and $36''$ respectively, and a Fourier-transform spectrometer covering the range $194\text{--}671\text{ }\mu\text{m}$ (Griffin et al. 2010). PACS consisted of a photometer which could observe at $160\text{ }\mu\text{m}$ and either 70 or $100\text{ }\mu\text{m}$ simultaneously, and a spectrometer covering $55\text{--}210\text{ }\mu\text{m}$ (Poglitsch et al. 2010). The Herschel Gould Belt Survey (HGBS) used the SPIRE and PACS photometers in ‘parallel mode’, mapping all three SPIRE bands and the PACS 70 and $160\text{ }\mu\text{m}$ bands simultaneously, although the fast scanning speed ($60''/\text{s}$) prevented the PACS data from being taken at optimal resolution, and resulted in a substantially elliptical PACS beam: $5.8'' \times 12.1''$ and $11.6'' \times 15.4''$ at $70\text{ }\mu\text{m}$ and $160\text{ }\mu\text{m}$ respectively (Poglitsch et al. 2010).

Parallel mode observations were taken in a scanning observing mode (referred to as scan-map mode in Herschel documentation). Each field was mapped twice, with orthogonal scan directions. The two scans were reduced separately, and then co-added. This procedure was used in order to minimise the effect of $1/f$ noise, which will introduce a slowly-varying component into the detector time series, on the output map (see e.g., the SPIRE Data Reduction Guide 2014).

Herschel data are typically reduced using the Herschel Interactive Processing Environment (HIPE; Ott 2010). Different methods are applied for the reduction of SPIRE and PACS data.

2.2.1 SPIRE Data Reduction

The data reduction process for SPIRE is described in detail in the SPIRE Data Reduction Guide (2014), and summarised here. SPIRE data are processed to one of a number of levels:

- Level 0** Raw time series data
- Level 0.5** Time series data calibrated in physical units
- Level 1** Processed time series data calibrated in Jy beam^{-1}
- Level 2** Flux calibrated maps for signal, error and coverage

The first step in the reduction process is to convert Level 0 (raw) data into physical units (Level 0.5 data). In order to process the data to Level 1, corrections are then applied to the time series: correcting for interference between detector components; accounting for bolometer drifts and temperature jumps; identifying and removing glitches caused by cosmic rays; correcting for low-pass filtering of the data; converting the data into astrophysical units; and finding and correcting ‘cooler burps’ (SPIRE recycled coolant on approximately a 2-day cycle; a cooler burp is a steep temperature rise which reaches a plateau 6 or 7 h after the end of such a cycle). Pointing

angles on the sky are determined for the detector time-lines. For regions dominated by extended emission, such as those in this work, an extended emission gain factor must be applied to each bolometer time series. These gain factors represent the ratio of the response of each bolometer to extended emission and the average response.

Taking the data from Level 1 to Level 2 is the ‘mapmaking’ step. The default mapmaking mode for SPIRE, known as ‘naïve’ mapmaking, is to project the full power seen by each detector into the nearest map pixel. Signal, signal squared and coverage maps are created. For each bolometer series at each time step in the observation, the signal measurement is added to the signal map, the signal measurement squared is added to the signal squared map, and 1 is added to the coverage map. The signal map is then divided by the coverage map, in order to return a flux density map (a mean signal map). The signal squared, signal, flux density and coverage maps are used to create a variance map, the square root of which is the error map. While this process can be performed in a non-iterative manner, it is generally necessary to iteratively ‘destripe’ SPIRE data. This process removes zero-level offsets in the bolometer time series by creating an average ‘map’ time series from the Level 2 signal map, determining the differences between this timeline and each individual bolometer time series, subtracting these offsets, and repeating the process until convergence between the map time series and each of the bolometer time series is reached. The destriping convergence parameter χ^2 is given, for the i th iteration of the destriper, by

$$\chi_i^2 = \sum_j ([\text{Map Timeline}]_i - [\text{Input Signal Timeline}]_j + [\text{Offset}]_{i,j})^2 \quad (2.7)$$

where $[\text{Map Timeline}]_i$ is the average map time-line for iteration i , $[\text{Input Signal Timeline}]_j$ is the input bolometer time series for the j th bolometer, and $[\text{Offset}]_{i,j}$ is the zero-level offset determined between the i th average map time-line and the j th bolometer time series. Note that this is not the usual definition of the χ^2 parameter, but we use this notation to be consistent with Herschel documentation. Convergence is deemed to be reached when the difference between χ^2 values in two successive iterations is less than a specified value. The standard condition for destriper convergence is

$$|\chi_i^2 - \chi_{i-1}^2| < 1 \times 10^{-10}. \quad (2.8)$$

The destriping process is described in detail in the SPIRE Data Reduction Guide (2014).

SPIRE data are by default mapped onto 6'', 10'' and 14'' pixels at 250 μm , 350 μm and 500 μm respectively, and are calibrated in units of Jy beam^{-1} . The maps can be converted into surface brightness units using the effective beam areas listed in Table 2.3.

Table 2.3 Herschel beam properties. PACS beam sizes are given for a telescope scanning speed of $60'' \text{ s}^{-1}$. SPIRE effective beam areas are for conversion between ‘per-beam’ units and surface brightness units.

	PACS		SPIRE		
	70 μm	160 μm	250 μm	350 μm	500 μm
Primary beam FWHM (arcsec)	5.8×12.1	11.6×15.4	18.1	25.2	36.6
Effective beam area (sq. arcsec)	–	–	447	816	1711
Detectors	64×32	32×16	139	88	43

2.2.2 PACS Data Reduction

The data reduction process for PACS is structured similarly to the process for SPIRE, and is described in detail in the PACS Data Reduction Guide: Photometry (2014). In processing PACS data from Level 0.5 to Level 1, corrections include calibration into astrophysical units; masking bad and saturated pixels; a flat field correction; a non-linearity correction, as PACS bolometers display a non-linear response for flux densities greater than 100 mJy/beam in all bands; and removal of glitches caused by cosmic rays.

Processing Level 1 time series data into a map can be performed in HIPE. However, HGBS PACS mapmaking is performed using the *Scanamorphos* map-maker (Roussel 2013), written in the Interactive Data Language (IDL). This algorithm uses the multiple detections of each observing position (both within one scan, and in the orthogonal repeat observation) to model and subtract thermal and non-thermal low-frequency drifts in the bolometer time series (assuming a constant underlying source signal, similar to the AST model in SCUBA-2 data reduction). Scanamorphos additionally detects and masks glitches and brightness discontinuities, before making a map projection where, as with SPIRE data reduction, the full power of each detector is projected into the nearest map pixel.

PACS data are by default calibrated in units of Jy pixel^{-1} , and are mapped onto $3''$ pixels.

2.2.3 Absolute Calibration of Herschel Data

SPIRE and PACS detectors are sensitive to relative variations in signal, and so the absolute calibration of the Herschel maps is determined by comparison to the all-sky maps produced by the Planck satellite (Planck Collaboration 2011). The maps used to calculate the Herschel calibrations are those taken by the Planck High Fre-

quency Instrument (Planck-HFI; Planck HFI Core Team 2011). Planck-HFI is itself calibrated relative to the sky brightness measured by COBE-FIRAS at the Galactic poles (Planck Collaboration 2014, and references therein).

Planck-HFI has two channels overlapping with the SPIRE wavebands: 545 GHz (550 μm) and 857 GHz (350 μm). Differences in filter profiles and central wavelengths between the SPIRE and Planck-HFI bands are accounted for using scalings which are applied to the Planck data. These scalings, described in detail in the SPIRE Handbook (2014), require an assumption about the shape of the underlying spectral energy distribution of the large-scale ISM emission. The typical assumption used in calculating scaling factors is that the ISM emission can be represented across the Herschel wavelengths by a modified blackbody distribution, i.e.

$$I_\nu \propto \nu^\beta B_\nu(T) \quad (2.9)$$

where I_ν is the ISM emission at frequency ν , β is the dust emissivity spectral index and $B_\nu(T)$ is the Planck function,

$$B_\nu(T) = \frac{2h\nu^3}{c^2} (e^{h\nu/k_B T} - 1)^{-1}. \quad (2.10)$$

This requires assumptions both about the temperature and the dust properties of the ISM. The standard background offsets used by the HGBS are 27.7, 159.8, 169.6, 94.4 and 41.1 MJy/sr at 70 μm 160 μm 250 μm 350 μm and 500 μm respectively, as determined by Bernard et al. (2010).

The primary point source calibrator for the Herschel photometers is Neptune. Point source calibration uncertainty for the SPIRE bands is $\lesssim 5\%$, and is dominated by the uncertainty in the model of Neptune’s submillimetre flux (Bendo et al. 2013). For extended sources, the SPIRE calibration accuracy is $\lesssim 10\%$ (Griffin et al. 2013). The point source calibration uncertainty of PACS is 3% at 70 μm and 5% at 160 μm (Balog et al. 2014; Müller et al. 2014). Extended source calibration accuracy for PACS is uncertain; the HGBS typically adopts calibration uncertainties of 10% and 20% at 70 μm and 160 μm respectively (e.g. Könyves et al. 2015).

2.3 IRAM 30m Telescope

The Institut de Radioastronomie Millimétrique (IRAM) 30-m telescope is a 30m single-dish parabolic antenna located on Pico Veleta in the Spanish Sierra Nevada. The telescope has various heterodyne receivers as well as continuum cameras operating at 3, 2, 1, and 0.9 mm. The IRAM 30m observations of the $\text{N}_2\text{H}^+(1-0)$ transition at $\sim 3\text{mm}$ used in this work are presented in André et al. (2007). The observations were taken using four SIS (superconductor-insulator-superconductor) heterodyne receivers simultaneously, with an autocorrelation spectrometer as a backend. The FWHM of the IRAM 30m beam at 3 mm is $26''$.

2.4 SCUBA-2 and Herschel Compatibility

2.4.1 Spatial Filtering

In order to make meaningful comparisons between SCUBA-2 and Herschel data, the large-scale structure to which SCUBA-2 is not sensitive must be removed from the Herschel observations. This is accomplished using the method developed by Sadavoy et al. (2013). Herschel data are added to the SCUBA-2 bolometer time series for a SCUBA-2 observation which has previously been reduced in the normal manner. The Herschel observations are scaled by a multiplicative factor such that they represent a small but non-negligible perturbation to the SCUBA-2 signal. The data reduction process is then repeated, using the same set of parameters which were used in the original reduction of the field. The original SCUBA-2 reduction of the data is then subtracted from the Herschel+SCUBA-2 map, leaving the spatially-filtered Herschel signal. Finally, the scaling applied the Herschel observation is reversed. For Herschel data ‘H’ scaled by a factor α and SCUBA-2 data ‘S2’, the filtering process can be summarised as

$$\text{Filtered Map} = \frac{\text{Map}(S2 + \alpha H) - \text{Map}(S2)}{\alpha}. \quad (2.11)$$

This process can be used either for a field for which both Herschel and SCUBA-2 data exist, or to create SCUBA-2-like observations for a field observed by Herschel alone. In the latter case, the SCUBA-2 field chosen as a background must contain minimal emission, and an automask reduction must be performed. In the former case—that of this work—the external mask applied to the SCUBA-2 reduction must also be applied to the Herschel data, in order to make the two observations of the field comparable. When the spatial filtering process is performed on a field for which there is both SCUBA-2 and Herschel data, the process will be repeated once for each SCUBA-2 observing position for which there are corresponding Herschel data, and the resulting spatially-filtered maps will then be combined to form a mosaic.

The effect of spatial filtering on Herschel data is shown in Fig. 2.12. This shows the SPIRE 250 μm map of the L1688 region of Ophiuchus, before and after being passed through the SCUBA-2 data reduction pipeline, using IR1 data reduction parameters and the mask shown in Fig. 2.8. The bottom panel of Fig. 2.12 shows the difference of the original and filtered maps, showing the extended emission which is lost in the filtering process.

2.4.2 Common-Resolution Convolution Kernels

In order to compare two telescope data sets, the two data sets must be brought to a common resolution. Each data set will have a resolution, and a beam pattern, determined by the instrument point spread function (PSF) at the wavelength under

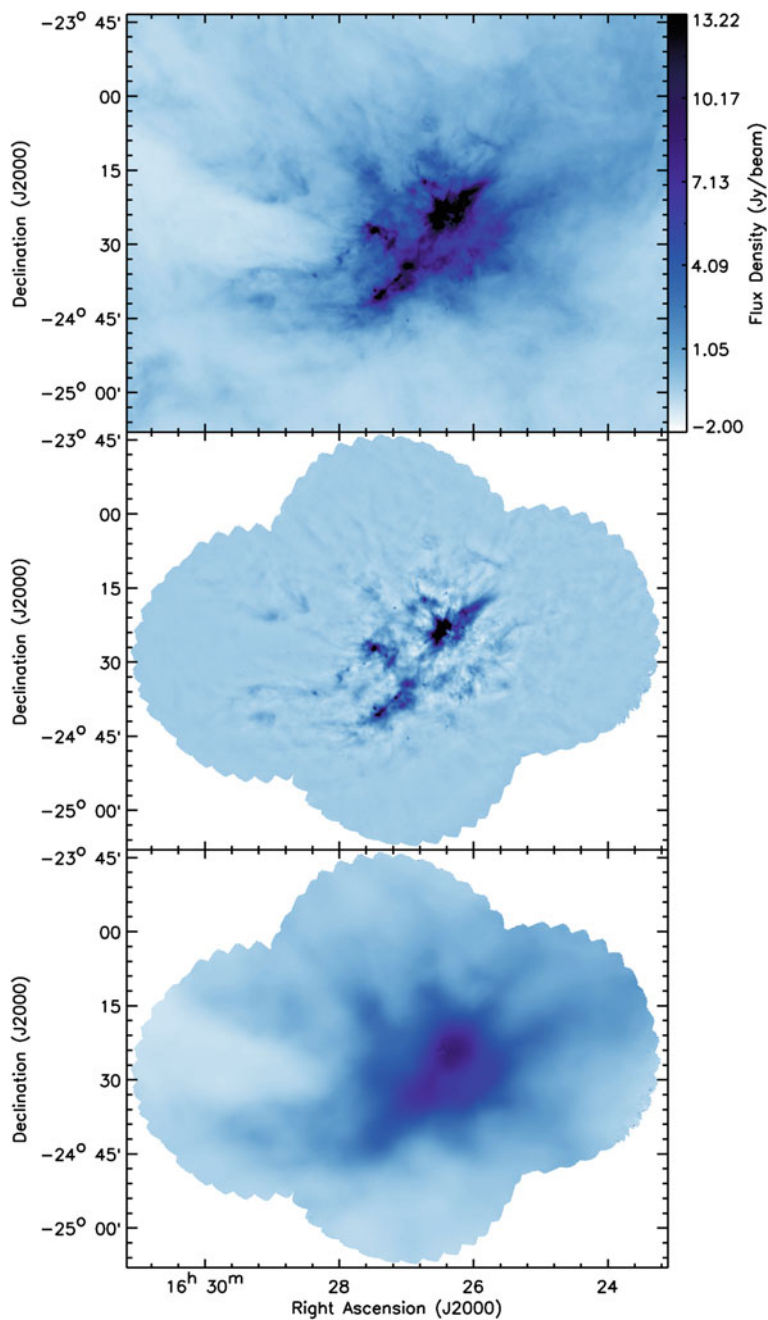
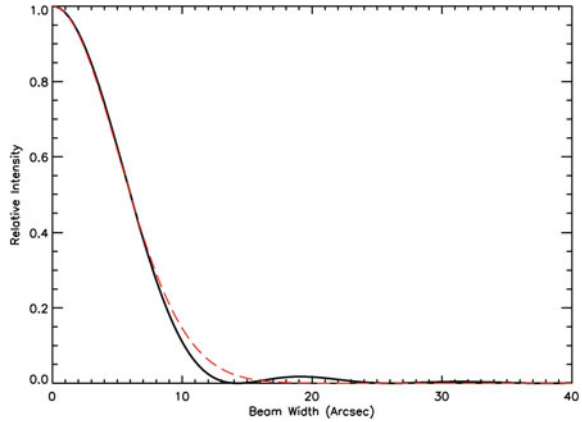


Fig. 2.12 The effect of spatial filtering on the SPIRE 250 μm map of L1688. *Top panel* SPIRE map. *Middle panel* Filtered map. *Bottom panel* Difference map. The same colour scaling applies to all panels

Fig. 2.13 Fraunhofer diffraction pattern for a 15 m-diameter aperture at 850 μm . Overlaid in red is a 12'' FWHM Gaussian distribution, for purposes of comparison



consideration. Typically, the data set at the higher resolution (that with the narrower PSF) must have a smoothing function applied in order to match the resolution of the other data set. Each of the SCUBA-2 and Herschel photometric bands used here has a different point spread function. In order to reconstruct the lower-resolution beams as accurately as possible, for the results presented in this work, convolution kernels were constructed. This section discusses the methods considered for bringing the SCUBA-2 and Herschel data sets to a common resolution, and describes the method decided upon in detail.

The Fraunhofer diffraction pattern formed by plane waves from a point source passing through a circular aperture will be an Airy disc; a radially symmetric pattern with a bright central peak, with successive maxima and minima of emission at increasing radii (see, e.g. Hecht 2001). The intensity I of an Airy disc at diffraction angle θ is given by

$$I(\theta) = I_0 \left(\frac{2J_1(x)}{x} \right)^2 \quad (2.12)$$

where I_0 is the peak intensity of the distribution, J_1 is a first-order Bessel function of the first kind, and the dimensionless parameter x is

$$x = \frac{\pi D}{\lambda} \sin \theta \quad (2.13)$$

where D is the aperture diameter and λ is the wavelength of the incoming light. The Airy diffraction pattern for light at 850 μm for a telescope with a diameter of 15 m is shown in Fig. 2.13. As shown in Fig. 2.13, the central maximum of an Airy disc can be well-approximated by a Gaussian distribution, and the primary beam width of a telescope is typically given as a Gaussian FWHM.

The resolution of a diffraction-limited circular aperture is determined by Rayleigh's criterion: two sources are considered marginally resolved when the cen-

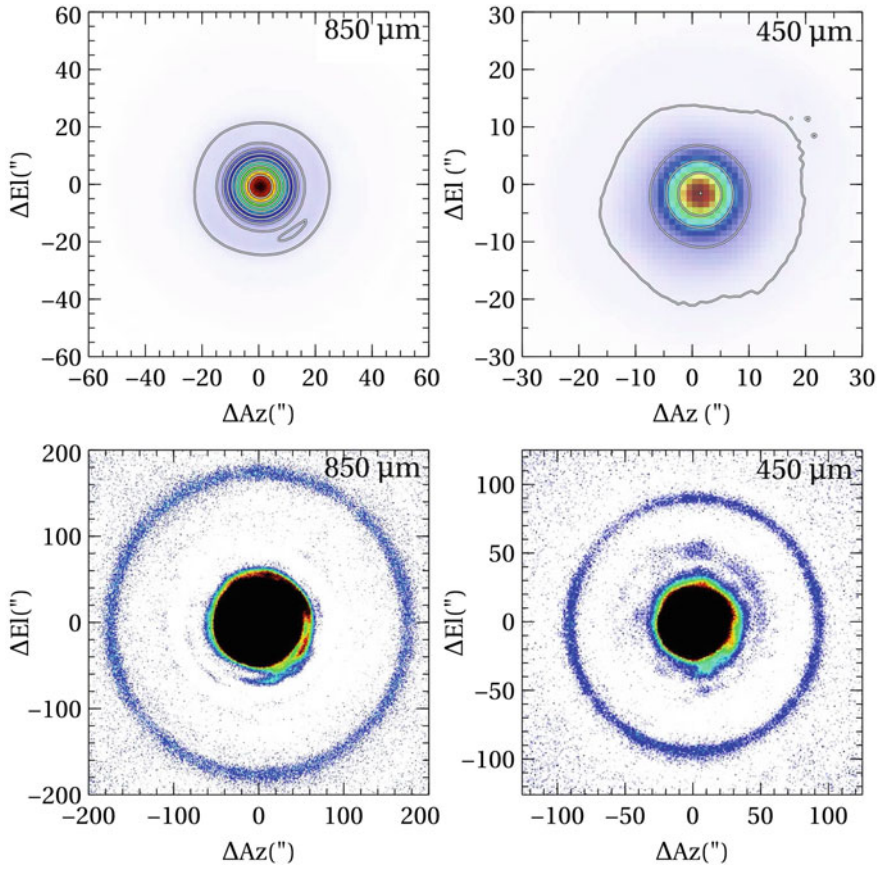


Fig. 2.14 SCUBA-2 450 and 850 μm coadded observations of Uranus. Dempsey et al. (2013), “SCUBA-2: on-sky calibration using submillimetre standard sources”, *Monthly Notices of the Royal Astronomical Society*, vol. 430, p. 2534, Figure 4. Reproduced with the permission of Oxford University Press

tral maximum of one source falls on the first minimum of the other. The angular separation of the first minimum from the central maximum in an Airy disc is

$$\theta = 1.22 \frac{\lambda}{D} \quad (2.14)$$

where λ is the wavelength of the light and D is the diameter of the aperture, i.e. the diameter of the telescope’s primary antenna.

In practice, no telescope beam is a perfect Airy disc. In the case of a reflecting telescope, obscuration of the primary mirror by the secondary focus and its supporting struts, as well as deformation of the primary mirror and other imperfections in the optical system, will alter the beam pattern. For ground-based telescopes such as the

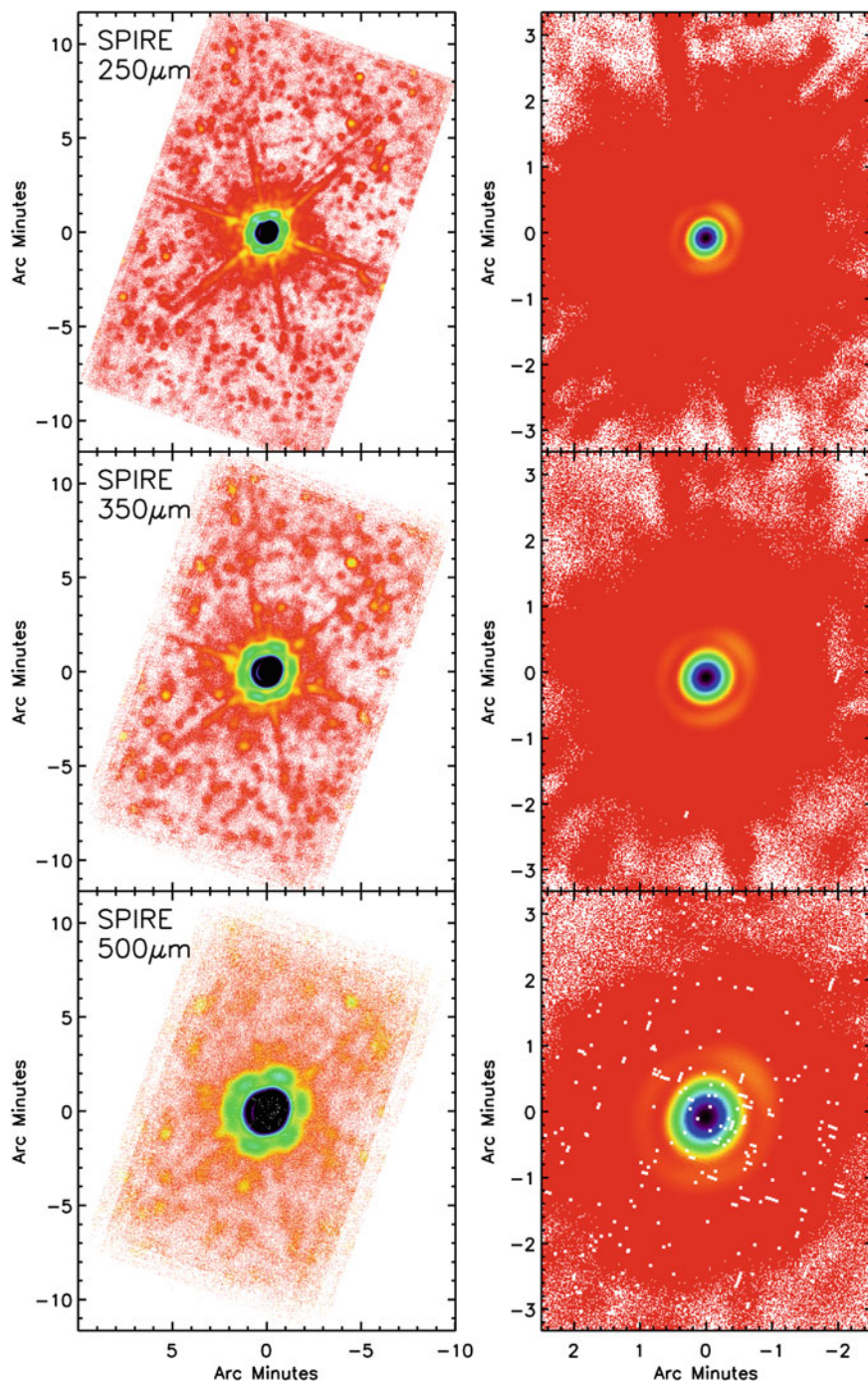


Fig. 2.15 SPIRE beam patterns, square-root scaled

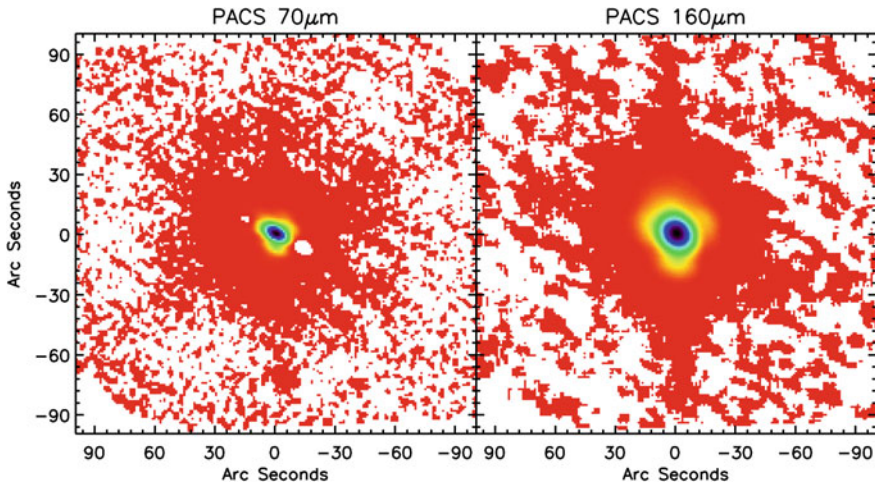


Fig. 2.16 PACS beams at $60'' \text{ s}^{-1}$ scanning speed, square-root scaled

JCMT, the atmospheric seeing will alter the beam pattern. The PSF of a telescope is determined in practice by observations of standard calibrators. The beam patterns, or point spread functions, of the JCMT at 450 and $850 \mu\text{m}$ are shown in Fig. 2.14. The beam patterns of SPIRE at 250 , 350 and $500 \mu\text{m}$ are shown in Fig. 2.15; the diffraction pattern resulting from the struts supporting the secondary mirror can be seen. The PACS 70 and $160\text{-}\mu\text{m}$ parallel-mode ($60'' \text{ s}^{-1}$ scanning speed) beam patterns are shown in Fig. 2.16. The ellipticity of the beam pattern can be clearly seen.

2.4.2.1 Fourier Transform Operators

In order to map point spread function (PSF) A onto a lower-resolution PSF B , a convolution kernel $K(A \Rightarrow B)$ must be chosen, such that

$$\text{PSF}_B = K(A \Rightarrow B) * \text{PSF}_A. \quad (2.15)$$

The convolution kernel $K(A \Rightarrow B)$ is the function for which

$$\text{FT}[\text{PSF}_B] = \text{FT}[K(A \Rightarrow B)] \times \text{FT}[\text{PSF}_A] \quad (2.16)$$

where FT represents the Fourier Transform operator,

$$\text{FT}[f(x)] = \hat{f}(k) = \int_{-\infty}^{\infty} f(x) e^{-2\pi i k x} dx \quad (2.17)$$

and FT^{-1} represents the inverse Fourier Transform operator,

$$\text{FT}^{-1}[\hat{f}(k)] = f(x) = \int_{-\infty}^{\infty} \hat{f}(k) e^{2\pi i k x} dk. \quad (2.18)$$

Equation 2.16 follows from the definition of the convolution theorem. The convolution $f * g$ of functions $f(x)$ and $g(x)$ is defined to be

$$f * g \equiv \int_{-\infty}^{\infty} g(x') f(x - x') dx'. \quad (2.19)$$

If $f(x)$ and $g(x)$ have Fourier transforms $\hat{f}(k)$ and $\hat{g}(k)$ respectively, then Eq. 2.19 can be rewritten as

$$f * g = \int_{-\infty}^{\infty} g(x') \left[\int_{-\infty}^{\infty} \hat{f}(k) e^{2\pi i k (x - x')} dk \right] dx' \quad (2.20)$$

$$= \int_{-\infty}^{\infty} \hat{f}(k) \left[\int_{-\infty}^{\infty} g(x') e^{-2\pi i k x'} dx' \right] e^{2\pi i k x} dk \quad (2.21)$$

$$= \int_{-\infty}^{\infty} \hat{f}(k) \hat{g}(k) e^{2\pi i k x} dk \quad (2.22)$$

$$= \text{FT}^{-1}[\hat{f}(k) \hat{g}(k)] \quad (2.23)$$

$$= \text{FT}^{-1} [\text{FT}(f) \text{FT}(g)] \quad (2.24)$$

and hence,

$$\text{FT}(f * g) = \text{FT}(f) \times \text{FT}(g). \quad (2.25)$$

For our purposes, $f = \text{PSF}_A$, and we wish to choose $g = K(A \Rightarrow B)$ such that $f * g = \text{PSF}_B$. See, e.g., Riley et al. (2006), Chapter 13 for a derivation and discussion of these results.

2.4.2.2 Single-Gaussian Beam Models

If all of the telescope beams can be adequately modelled as single Gaussians, then a simple analytical solution exists for the convolution kernel, as the Fourier transform of a Gaussian is another Gaussian. For the case where

$$\text{PSF}_A \propto e^{-8 \ln 2 \left(\frac{r}{2 \text{FWHM}_A} \right)^2} \quad (2.26)$$

and

$$\text{PSF}_B \propto e^{-8 \ln 2 \left(\frac{r}{2 \text{FWHM}_B} \right)^2} \quad (2.27)$$

where r is the radial distance from the beam centre and $\text{FWHM}_B > \text{FWHM}_A$, the Gaussian FWHM width $\text{FWHM}_{A \rightarrow B}$ necessary to bring data set A to the resolution of data set B will be

$$\text{FWHM}_{A \rightarrow B} = \sqrt{(\text{FWHM}_B)^2 - (\text{FWHM}_A)^2} \quad (2.28)$$

as Gaussians add in quadrature. Then, the Gaussian function which maps A onto B will be

$$K(A \Rightarrow B) = C e^{-8 \ln 2 (r/2 \text{FWHM}_{A \rightarrow B})^2} \quad (2.29)$$

where C is a normalisation constant. For example, a SCUBA-2 850- μm map at 14.1'' resolution would require smoothing with a 33.8'' Gaussian kernel to bring the map to the 36.6'' resolution of the Herschel-SPIRE 500- μm band.

SCUBA-2 450- μm fluxes have previously been noted to show an excess over the values expected from interpolation of the Herschel 160, 250, 350 and 500- μm bands (Sadavoy et al. 2013). This discrepancy was also seen in our data sets when they were brought to a common resolution by smoothing the lower-resolution maps with simple Gaussian kernels.

2.4.2.3 Double-Gaussian SCUBA-2 Beam Models

As approximating the beams as single Gaussians appears to result in the overestimation of 450- μm flux densities at 500- μm resolution, an alternative is to use the two-component Gaussian SCUBA-2 450 μm beam model described by Dempsey et al. (2013), and continue to approximate the Herschel beams as single Gaussians. In this case, one would typically cross-convolve both A and B to a common, lower, resolution, $A * B$.

In this model, to cross-convolve PSF_B with the two-component PSF_A , two Gaussian convolutions are needed. For the primary beam, the convolution needed is

$$K(A_{\text{primary}}) = C_{A,\text{primary}} e^{-8 \ln 2 (r/2 \text{FWHM}_{A,\text{primary}})^2} \quad (2.30)$$

and for the secondary beam, the same model applies. Then, the output map is given by

$$\begin{aligned} \text{PSF}_{A*B} = & (\text{Primary Beam Volume}) \times (K(A_{\text{primary}}) * \text{PSF}_B) + \\ & (\text{Secondary Beam Volume}) \times (K(A_{\text{secondary}}) * \text{PSF}_B). \end{aligned} \quad (2.31)$$

The SCUBA-2 450- μm primary and secondary beam volumes are listed in Table 2.1.

To convolve PSF_A with the single-component PSF_B , the convolution needed is

$$K(B) = C_B e^{-8 \ln 2 (r/2 \text{FWHM}_B)^2} \quad (2.32)$$

and the output map is given by

$$\text{PSF}_{B*A} = K(B) * \text{PSF}_A. \quad (2.33)$$

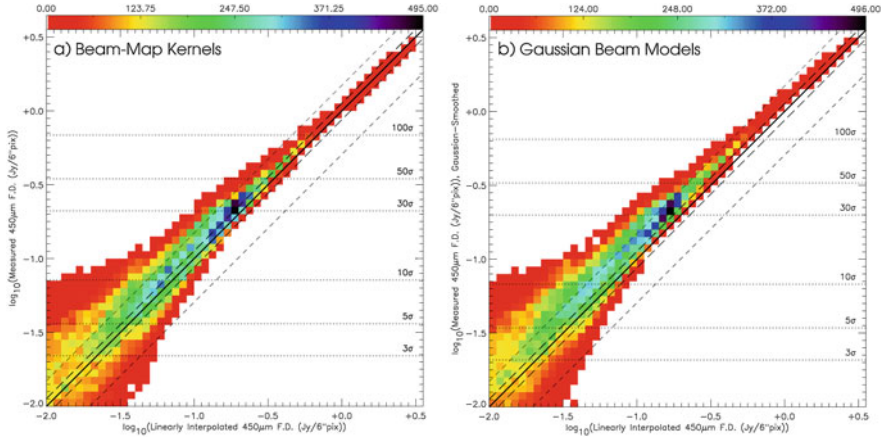


Fig. 2.17 Histograms showing the agreement between predicted and measured 450- μm flux densities in the CO-subtracted region of L1688, for maps brought to a common resolution using (a) the beam-map convolution kernels and (b) double-Gaussian model for the 450- μm beam. Colour scale shows the number of map pixels in each box in the grid. Thick black lines show 1:1 agreement; long-dashed lines show 13% calibration error; short-dashed lines show 50% calibration error

Note that convolution is a commutative process, so $\text{PSF}_{A*B} = \text{PSF}_{B*A}$. However, when this model is applied to SCUBA-2 450- μm and Herschel 500- μm data, it proves not to be a good enough approximation, as, as shown in Fig. 2.17, it does not remove the 450- μm excess seen at 500- μm resolution.

2.4.2.4 Beam-Map Convolution Kernels

As a part of this work, a set of convolution kernels were made using the Herschel and SCUBA-2 beam maps, following the method of Aniano et al. (2011). This was done to test the hypothesis that the apparent 450- μm excess was caused by the approximation of the 450- μm beam secondary component as a Gaussian (Dempsey et al. 2013). The method described by Aniano et al. (2011) can be applied to either measured beam maps or model telescope beams, and involves constructing a convolution kernel $K(A \Rightarrow B)$ empirically. In principle, $K(A \Rightarrow B)$ is derived using

$$K(A \Rightarrow B) = \text{FT}^{-1} \left(\frac{\text{FT}(\text{PSF}_B)}{\text{FT}(\text{PSF}_A)} \right). \quad (2.34)$$

In practice, however, the division by $\text{FT}(\text{PSF}_A)$ leads to $K(A \Rightarrow B)$ being dominated by noise, unless the high-frequency (i.e. high wavenumber k) components of PSF A are filtered. Firstly, high-frequency noise is filtered from both PSFs using a filter ϕ which takes the form

$$\phi(k) = \begin{cases} 1 & \text{for } k \leq k_\alpha \\ \exp\left(-\left(1.8249 \times \frac{k-k_\alpha}{k_\beta-k_\alpha}\right)^4\right) & \text{for } k_\alpha < k \leq k_\beta \\ 0 & \text{for } k_\beta < k \end{cases} \quad (2.35)$$

where $k_\alpha = 0.9k_\beta$ and $k_\beta = 8\pi/\text{FWHM}$ where FWHM is the FWHM of the instrument primary beam. Hereafter, $\text{FT}_\phi = \phi \times \text{FT}$. The highest-frequency components of PSF A are further filtered: Eq. 2.34 becomes

$$K(A \Rightarrow B) = \text{FT}^{-1} \left(\frac{\text{FT}_\phi(\text{PSF}_B)}{\text{FT}_\phi(\text{PSF}_A)} \times f_A \right) \quad (2.36)$$

and the filter f_A takes the form

$$f_A(k) = \begin{cases} 1 & \text{for } k \leq k_{L,A} \\ \frac{1}{2} \left(1 + \cos\left(\pi \times \frac{k-k_{L,A}}{k_{H,A}-k_{L,A}}\right) \right) & \text{for } k_{L,A} < k \leq k_{H,A} \\ 0 & \text{for } k_{H,A} < k \end{cases} \quad (2.37)$$

where $k_{H,A}$ is the highest wavenumber at which $\text{FT}(\text{PSF}_A)$ is appreciable:

$$\text{FT}(\text{PSF}_A)(k_{H,A}) = 0.005 \times \text{FT}(\text{PSF}_A)_{\text{max}} \quad (2.38)$$

and $k_{L,A} = 0.7k_{H,A}$. Prior to constructing the convolution kernel, the PSFs are centroided, resampled to a common grid of $3645 \times 3645 \times 0.2''$ pixels, and circularly averaged. The SCUBA-2 and SPIRE beams are already approximately circular and are largely unchanged by this circular averaging. The PACS beams, which are substantially elliptical in parallel-mode observations (see Fig. 2.16), are more affected, and the convolution process may produce some distortion in convolved 70 and 160- μm maps. However, as both the circular averaging process and the convolution process conserve flux, provided that the PACS beams are smaller along both their axes than the beam to which they are being convolved, then total beam-map-kernel-convolved PACS flux densities measured inside an aperture the same size as or larger than the target beam size will be accurate. It should also be noted that all of the SCUBA-2, SPIRE and PACS instruments scan in more than one direction on the sky while taking an observation, and hence the beam pattern is rotated several times within each observation. This means that the beam pattern is to some extent circularly averaged even before the convolution is applied.

The kernels created for this work were generated using a routine written in Interactive Data Language (IDL), implementing the method described above. The SPIRE and PACS beam maps shown in Figs. 2.15 and 2.16 were used as input for the Herschel beam patterns. SCUBA-2 beam maps were generated by co-adding high-quality calibration observations of Uranus taken at 450 and 850 μm . Convolutions

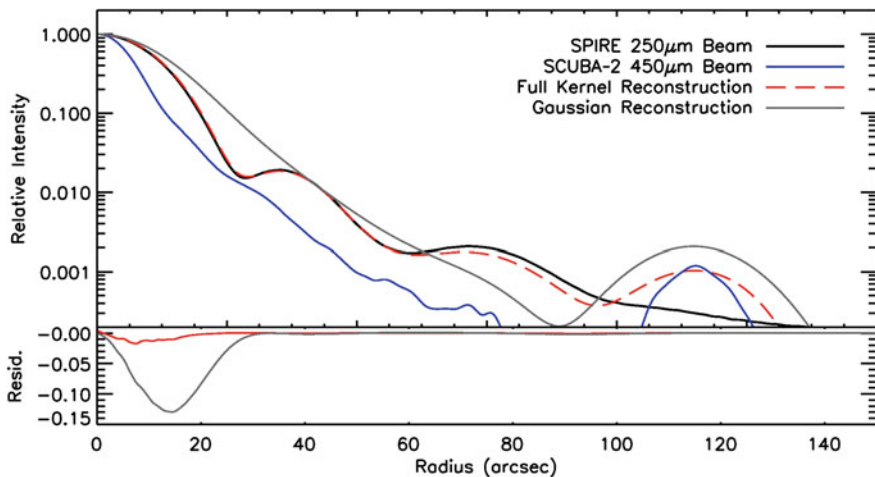


Fig. 2.18 Comparison between the beam-map kernel (*red*) and single-Gaussian (*grey*) reconstructions of the SPIRE 250- μm beam (*black*) from the SCUBA-2 450- μm beam (*blue*). Residuals are shown below. This figure appears in Pattle et al. (2015), Monthly Notices of the Royal Astronomical Society, vol. 450, p. 1094

were performed using a separate routine, also written in IDL, supplied by Aniano et al. (2011).

Using the convolution kernels improves reconstruction of the beam, as shown in Fig. 2.17. These plots compare the measured SCUBA-2 450- μm flux density for each pixel in the map (y axis) to the 450- μm flux density predicted by linear interpolation between the SPIRE 350- μm and SPIRE 500- μm data for the same pixel (x axis). Figure 2.17a shows this at SPIRE 500- μm resolution, for maps convolved using the beam-map kernels described above. Figure 2.17b shows this at (SPIRE 500- μm * SCUBA-2 450- μm) resolution, with maps smoothed using the double-Gaussian beam model for the SCUBA-2 450- μm beam described above, and a single-Gaussian beam model for the SPIRE 350- μm and 500- μm beams. Both with and without the convolution kernels, there is a clear upward skew to the distribution of measured against predicted 450- μm flux densities, particularly at lower signal-to-noise. However, in Fig. 2.17b, a systematic offset from the 1:1 line can be seen at the highest signal-to-noise values. This offset is not seen in Fig. 2.17a, and in Fig. 2.17a, the upward skew is less pronounced. This suggests that use of the beam-map convolution kernels improves reconstruction of the lower-resolution beams from the 450- μm beam, without entirely resolving the issue. It must be noted that the low-power portions of the 450- μm beam at large radii are substantially affected by atmospheric conditions, and hence are likely to vary between observations. Any beam model or average beam map must necessarily be an approximation to the true beam pattern when the observations were taken.

An example of the reconstruction of a beam using the beam-map convolution kernels is shown in Fig. 2.18. The reconstruction of the SPIRE 250- μm beam from

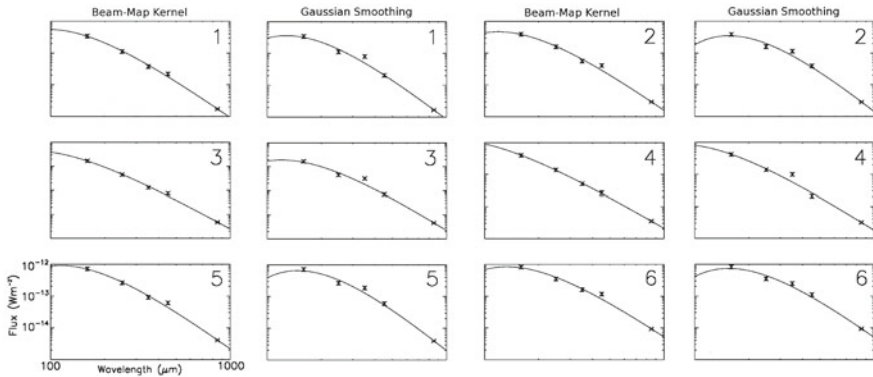


Fig. 2.19 Some example SEDs for sources detected in the L1688 region of Ophiuchus. The *left-hand columns* show the fluxes measured when the data are convolved to SPIRE 350- μm resolution using the beam-map kernels. The *right-hand columns* show the fluxes measured when the data are convolved to SPIRE 350- μm resolution using single-Gaussian beam models. Axis values and ranges are the same in all panels, and as shown in the lower-left-hand panel

the SCUBA-2 450- μm beam is shown, along with the beam reconstruction resulting from treating both beams as single Gaussians. Note the flux excess resulting from approximating the beams as single Gaussians (grey line in main plot and residuals). The second and third Airy peaks of the SPIRE beam are recovered well using the beam-map kernel.

The improvement in agreement between fluxes measured at different wavelengths through use of beam-map kernels is shown in Fig. 2.19. This figure shows some example SEDs for sources detected in the L1688 region of Ophiuchus, brought to SPIRE 350- μm resolution using beam-map kernels (left-hand columns) and brought to (SPIRE 350- μm * SCUBA-2 450- μm) resolution using a double-Gaussian beam model for the SCUBA-2 450- μm beam and single-Gaussian beam models for the other beams (right-hand columns). At (SPIRE 350- μm * SCUBA-2 450- μm) resolution, the Gaussian model typically causes an apparent excess at 350 μm —as opposed to (SPIRE 500- μm * SCUBA-2 450- μm) resolution, where the apparent excess is seen at 450 μm —see Fig. 2.17. This excess is removed by convolving the data to a common resolution using the beam map kernels, although a slight 450- μm excess typically then becomes apparent in the beam-map-kernel-convolved maps. This is not surprising, since, as discussed above, the beam-map kernels do not entirely account for the variations in the SCUBA-2 450- μm beam, and SCUBA-2 450- μm fluxes remain slightly above their predicted values.

2.5 Summary

We have introduced and discussed the telescopes with which data used in this work were taken: the James Clerk Maxwell Telescope (JCMT), the Herschel Space Observatory and the IRAM 30-m telescope. We discussed the SCUBA-2 and HARP instruments on the JCMT, and the SPIRE and PACS instruments on Herschel. We discussed methods by which data from SCUBA-2 and Herschel can be meaningfully compared.

The JCMT is a 15m-diameter submillimetre telescope located at the summit of Mauna Kea. Data taken using two instruments on the JCMT—the camera SCUBA-2 and the heterodyne receiver HARP-B—are used in this work. SCUBA-2 is a 10000-pixel submillimetre camera which takes data simultaneously at 450 and 850 μm , with effective resolutions of 9.6'' and 14.1'' respectively. HARP-B is a 16-pixel heterodyne receiver which operates in the frequency range 325–375 GHz (~ 800 –925 μm), with an angular resolution of 14'' at 345 GHz.

SCUBA-2 data reduction requires iterative modelling of the astrophysical and atmospheric signal received by the telescope, as well as correlated low-frequency noise. In order to prevent atmospheric signal being spuriously assigned as astrophysical emission in low signal-to-noise regions, a signal-to-noise based ‘mask’ is used to define regions of significant astrophysical emission. In order to avoid the necessity for a priori knowledge of the astrophysical signal, the data reduction process is repeated twice. Firstly, the mask is defined based on simple signal-to-noise cuts in each iteration. A mask is then defined based on a signal-to-noise cut in the co-added and mosaiced first set of reductions. The fields observed are then re-reduced using this mask.

The SCUBA-2 850- μm window can be significantly contaminated by the CO $J=3 \rightarrow 2$ transition. Where the ^{12}CO emission in a SCUBA-2 field has been observed with HARP-B, this is corrected for by re-reducing the SCUBA-2 data with the integrated HARP-B ^{12}CO emission included as a negative signal.

Herschel was a 3.5 m-diameter submillimetre space observatory, observing in the wavelength range 70–500 μm . Data taken using the SPIRE and PACS photometers are used in this work. SPIRE observed at 250, 350 and 500 μm , at resolutions of 18'', 25'' and 36'' respectively. Data were taken simultaneously using the PACS photometer, operating at 70 and 160 μm , at resolutions of $5.8'' \times 12.1''$ and $11.6'' \times 15.4''$ respectively.

The IRAM 30-m telescope is a 30 m-diameter millimetre telescope located on Pico Veleta. The telescope operates in the wavelength range ~ 0.9 –3 mm, and has both continuum and heterodyne observing modes. IRAM 30 m observations of the $\text{N}_2\text{H}^+ J=1 \rightarrow 0$ transition at 3 mm are used in this work.

Due to the necessity of removing atmospheric signal from SCUBA-2 data, SCUBA-2 is not sensitive to emission on spatial scales larger than its own array size (600''), and further spatial filtering is introduced by the mask used to constrain the data reduction process. In order to compare SCUBA-2 and Herschel data, it is necessary to spatially filter the Herschel data in the same manner as the SCUBA-2 data. This is done by re-reducing a SCUBA-2 field with the Herschel observations

of the same region included, scaled to be a small perturbation on the SCUBA-2 data. The original SCUBA-2 reduction of the field is then subtracted, leaving the filtered Herschel data.

When bringing SCUBA-2 and Herschel data to a common resolution, it is necessary to use convolution kernels based on the true telescope beams, rather than Gaussian approximations. The SCUBA-2 450- μm beam, in particular, has a substantial fraction of its power in the secondary beam, and cannot be modelled adequately as either a single- or a double-Gaussian, for the purposes of convolving the data to a common resolution with a Herschel data set. The empirically-derived convolution kernels used in this work significantly improve the previously-noted discrepancies between Herschel and SCUBA-2 450- μm flux densities.

References

- André, P., Belloche, A., Motte, F., & Peretto, N. (2007). *Astronomy and Astrophysics*, 472, 519.
- Aniano, G., Draine, B. T., Gordon, K. D., & Sandstrom, K. (2011). *Publications of the Astronomical Society of the Pacific*, 123, 1218.
- Balog, Z., Müller, T., Nielbock, M., et al. (2014). *Experimental Astronomy*, 37, 129.
- Bendo, G. J., Griffin, M. J., Bock, J. J., et al. (2013). *Monthly Notices of the Royal Astronomical Society*, 433, 3062.
- Bernard, J.-P., Paradis, D., Marshall, D. J., et al. (2010). *Astronomy and Astrophysics*, 518, L88.
- Bolatto, A. D., Wolfire, M., & Leroy, A. K. (2013). *Annual Review of Astronomy and Astrophysics*, 51, 207.
- Buckle, J. V., Hills, R. E., Smith, H., et al. (2009). *Monthly Notices of the Royal Astronomical Society*, 399, 1026.
- Chapin, E. L., Berry, D. S., Gibb, A. G., et al. (2013). *Monthly Notices of the Royal Astronomical Society*, 430, 2545.
- Currie, M. J., Draper, P. W., Berry, D. S., et al. (2008). In R. W. Argyle, P. S. Bunclark, & J. R. Lewis (Eds.), *Astronomical data analysis software and systems XVII*. Astronomical society of the pacific conference series (Vol. 394, p. 650).
- Curtis, E. I., Richer, J. S., & Buckle, J. V. (2010). *Monthly Notices of the Royal Astronomical Society*, 401, 455.
- de Graauw, T., Helmich, F. P., Phillips, T. G., et al. (2010). *Astronomy and Astrophysics*, 518, L6.
- Dempsey, J. T., Friberg, P., Jenness, T., et al. (2013). *Monthly Notices of the Royal Astronomical Society*, 430, 2534.
- Drabek, E., Hatchell, J., Friberg, P., et al. (2012). *Monthly Notices of the Royal Astronomical Society*, 426, 23.
- Griffin, M. J., Abergel, A., Abreu, A., et al. (2010). *Astronomy and Astrophysics*, 518, L3.
- Griffin, M. J., North, C. E., Schulz, B., et al. (2013). *Monthly Notices of the Royal Astronomical Society*, 434, 992.
- Hecht, E. (2001). *Optics* (4th ed.). Addison-Wesley.
- Herschel Observers' Manual. (2014) Version 5.0.3, HERSCHEL-HSC-DOC-0876. Retrieved April 27, 2015 from <http://herchel.esac.esa.int/Docs/Herschel/pdf/observatory.pdf>.
- Holland, W. S., Bintley, D., Chapin, E. L., et al. (2013). *Monthly Notices of the Royal Astronomical Society*, 430, 2513.
- Jenness, T., Cavanagh, B., Economou, F., & Berry, D. S. (2008). In R. W. Argyle, P. S. Bunclark, & J. R. Lewis (Eds.), *Astronomical data analysis software and systems XVII*, Astronomical society of the pacific conference series (Vol. 394, p. 565).

- Könyves, V., André, P., Men'shchikov, A., et al. (2015). *Astronomy and Astrophysics*, 584, A91.
- Müller, T., Balog, Z., Nielbock, M., et al. (2014). *Experimental Astronomy*, 37, 253.
- Ott, S. (2010). In Y. Mizumoto, K.-I. Morita, & M. Ohishi (Eds.), *Astronomical data analysis software and systems XIX*, Astronomical society of the pacific conference series (Vol. 434, p. 139).
- PACS Data Reduction Guide: Photometry. (2014) Version 11. Retrieved March 28, 2015 from http://herschel.esac.esa.int/hcss-doc-13.0/print/pacs_phot/pacs_phot.pdf.
- Pattle, K., Ward-Thompson, D., Kirk, J. M., et al. (2015). *Monthly Notices of the Royal Astronomical Society*, 450, 1094.
- Pilbratt, G. L., Riedinger, J. R., Passvogel, T., et al. (2010). *Astronomy and Astrophysics*, 518, L1.
- Planck Collaboration. (2011). *Astronomy and Astrophysics*, 536, A1.
- Planck Collaboration. (2014). *Astronomy and Astrophysics*, 571, A8.
- Planck HFI Core Team. (2011). *Astronomy and Astrophysics*, 536, A4.
- Poglitsch, A., Waelkens, C., Geis, N., et al. (2010). *Astronomy and Astrophysics*, 518, L2.
- Riley, K. F., Hobson, M. P., & Bence, S. J. (2006). *Mathematical methods for physics and engineering* (3rd ed.). Cambridge University Press.
- Roussel, H. (2013). *Publications of the Astronomical Society of the Pacific*, 125, 1126.
- Sadavoy, S. I., Di Francesco, J., Johnstone, D., et al. (2013). *Astrophysics Journal*, 767, 126.
- SPIRE Data Reduction Guide. (2014) SPIRE-RAL-DOC 003248. Retrieved March 28, 2015 from http://herschel.esac.esa.int/hcss-doc-13.0/print/spire_drg/spire_drg.pdf.
- SPIRE Handbook. (2014) Version 2.5, HERSCHEL-DOC-0798. Retrieved March 28, 2015 from http://herschel.esac.esa.int/Docs/SPIRE/spire_handbook.pdf.

Submillimetre Studies of Prestellar and Starless Cores
in the Ophiuchus, Taurus and Cepheus Molecular
Clouds

Pattle, K.M.

2017, XVI, 254 p. 113 illus., 82 illus. in color., Hardcover

ISBN: 978-3-319-56519-4